Journal of Energy Chemistry 71 (2022) 392–399

Contents lists available at ScienceDirect

Journal of Energy Chemistry

journal homepage: www.elsevier.com/locate/jechem

http://www.journals.elsevier.com/journal-of-energy-chemistry/

Boosting the kinetics of PF_6^- into graphitic layers for the optimal cathode of dual-ion batteries: The rehearsal of pre-intercalating Li^+

He Yang [a], Tingting Qin [a], Xinyan Zhou [a], Yu Feng [a], Zizhun Wang [a], Xin Ge [a], Nailin Yue [a], Dabing Li [b], Wei Zhang [a,*], Weitao Zheng [a,*]

[a] Key Laboratory of Automobile Materials MOE, School of Materials Science & Engineering, Jilin Provincial International Cooperation Key Laboratory of High-Efficiency Clean Energy Materials, Electron Microscopy Center, and International Center of Future Science, Jilin University, Changchun 130012, Jilin, China
[b] State Key Laboratory of Luminescence and Applications, Changchun Institute of Optics, Fine Mechanics and Physics, Chinese Academy of Sciences, Changchun 130033, Jilin, China

ARTICLE INFO

Article history:
Received 10 March 2022
Revised 8 April 2022
Accepted 8 April 2022
Available online 15 April 2022

Keywords:
Dual-ion batteries
Anion intercalation
Kinetics
Pre-intercalation

ABSTRACT

Large anions exhibit slow diffusion kinetics in graphite cathode of dual-ion batteries (DIBs); particularly at high current density, it suffers severely from the largely-reduced interlayer utilization of graphite cathode, which as a bottleneck limits the fast charge application of DIBs. To maximize interlayer utilization and achieve faster anion diffusion kinetics, a fast and uncrowded anion transport channel must be established. Herein, Li^+ was pre-intercalated into the graphite paper (GP) cathode to increase the interlayer spacing, and then hosted for the PF_6^- anion storage. Combined with theoretical calculation, it shows that the local interlayer spacing enlargement and the residual Li^+ reduce the anion intercalation energy and diffusion barrier, leading to better rate stability. The obtained GP with Li^+ pre-intercalation (GP-Li) electrode exhibits a discharge capacity of 23.1 mAh g^{-1} at a high current of 1300 mA g^{-1}. This work provides a facile method to efficiently improve the interlayer utilization of graphite cathode at large currents.

1. Introduction

Dual-ion batteries (DIBs) are promising energy storage devices for their advantages of high energy density, low cost and environmental friendliness [1–3]. The energy storage mechanism of DIBs is different from the traditional rocking-chair batteries (e.g., lithium-ion battery, LIB) [4–6]. When charged, large anions (e.g., PF_6^- [7], $TFSI^-$ [8], FSI^- [9]) in electrolyte intercalate into the cathode, whereas cations (e.g., $EMIm^+$ [10,11], Li^+ [12–14], Na^+ [15–17]) move from the electrolyte to the anode. At the discharge process, both anions and cations move from the electrodes to the electrolyte.

Due to the high potential of anion intercalation, cathode materials with high voltage-resistance and accommodating large anions are seldom reported. Currently, the studies of DIB cathode materials are still on the selection of materials. Graphite provides a structural basis for anions intercalation and becomes the most typical cathode material for DIBs due to its superior chemical stability and Van der Waals force stacking between layers [18,19]. However, the size of intercalated anions (such as the minimum height of PF_6^- is 3.5 Å, of $TFSI^-$ is 3.8 Å) is comparably larger than the interlayer spacing of graphite (3.35 Å). The tight restacking structure of graphite triggers an irreversible expansion arising after cycles [20–22]. Recently, it has been reported that by modifying the electrolyte, a stable cathode–electrolyte interface can be established to enhance the stability, which, however, mainly focuses on the surface modification of materials [23–27]. Although the larger particle size can maintain the structural stability of graphitic cathode, the intrinsic extension of the anion diffusion path always leads to unsatisfactory ion diffusion kinetics [28–30]. Therefore, the anion intercalation occurs mainly at the edge and subsurface of graphite at high current densities, the ultra-low utilization of graphite and rate performance are always expected to be improved.

To maximize the interlayer utilization, it is supposed to establish a rapid and uncrowded anion transport channel to obtain the optimal anion diffusion process. Reducing the particle size and increasing the specific surface area of graphite, such as constructing porous graphite or nano-structural design [31–33], can effectively shorten the anion diffusion path, so as to enhance the anion diffusion kinetics. Nevertheless, these methods mainly rely on the adsorption–desorption of anions at a relatively lower potential, without accelerating the kinetics of anion shuttling between

* Corresponding authors.
E-mail addresses: weizhang@jlu.edu.cn (W. Zhang), wtzheng@jlu.edu.cn (W. Zheng).

https://doi.org/10.1016/j.jechem.2022.04.009

graphite layers substantially. In this case, the interlayer structure of graphite must be modified to reduce the interlayer resistance of (de)intercalation reaction with the overall graphite structure maintain. Pre-intercalation methods enable tuning the interlayer structure of graphite. However, the intercalated medium with a large size always generates excessive expansion and introduces a porous structure, making the improvement of ion diffusion mainly dependent on the electric double-layer process [34,35]. The pre-intercalation of small ions can effectively improve the electrochemical performance of graphite and ensure the layered structure [36,37]. Thus, it is ideal to use smaller-sized media in pre-intercalation to the minimum the damage to the targeting graphite layers.

Since towards maintaining the integrity of graphite structure, it is fundamentally challenging to considerably enlarge the interlayer spacing of graphite. Herein, aiming to accelerate the anions diffusion kinetics, the popular integrated graphite paper (GP) with high stability was used as a host material for PF_6^- storage. We demonstrate a proof-of-concept that using a simple self-discharge method, the minimum-sized pre-intercalation of Li^+ enables modifying the interlayer structure of GP. Delicate theoretical calculations prove that the interlayer spacing expansion and the residual minority of Li^+ reduce the anion intercalation energy and diffusion barrier, which enhance the PF_6^- diffusion kinetics. Thus, in 1 M [BMIm][PF_6] ionic liquid, the obtained Li^+ pre-intercalation GP (GP-Li) electrode gained a discharge capacity of 23.1 mAh g^{-1} at 1300 mA g^{-1}, and achieved an excellent capacity retention rate of 94.6% after 500 cycles. Our pre-treatment method provides a new perspective for facilitating the anions diffusion process.

2. Materials and methods

2.1. Reagents and materials

Graphite paper (GP, 0.05 mm) is supplied by Tanqianlang Materials. Li^+ secondary electrolyte and Li foil are provided by Dodo-Chem. Ionic liquid 1-butyl-3-methylimidazolium Hexafluorophosphate ([BMIm][PF_6]) (purity: 97%), 1-Butyl-3-methylimidazolium thiocyanate ([BMIm][TFSI]) (purity: 95%), propylene carbonate (PC) solution (purity: >98%) and ethyl methyl carbonate (EMC) solution (purity: 98%) are purchased from Aladdin Industrial Corporation. Highly oriented pyrolytic graphite (HOPG) is purchased from XFNANO.

2.2. Synthesis of Li^+ pre-intercalation graphite paper (GP-Li)

Li foil soaked with electrolyte was first covered on the surface of graphite paper, then a pressure was put on both sides. A potential difference arose between the Li foil and graphite paper interface, and then the self-discharge of Li foil was generated. Li^+ and electrons were released into the graphite paper. 3 h later, the graphite paper was removed and put into ethanol for ultrasonic cleaning, later dried at 60 °C in vacuum oven to obtain the Li^+ pre-intercalation graphite paper sample (GP-Li). The reaction equations for Li^+ pre-intercalation process are as follows: $Li - e^- \rightarrow Li^+$, $xLi + xe^- + C \rightarrow Li_xC$.

2.3. Characterizations

X-ray diffraction (XRD) measurements were performed by a powder diffractometer (RIGAKU D/MAX2500) in the reaction mode (Cu K_α radiation, λ = 1.5406 Å). Scanning electron microscopy (SEM) was recorded by a Hitachi SU8010 microscope with a field-emission gun. Raman spectra were collected with TESCAN RISE (S9000G). X-ray photoelectron spectroscopy (XPS) was conducted on a monochromatic Al $K\alpha$ radiation source (Thermofisher Scientific Company). Transmission electron microscopy (TEM) was carried out by JEM-2100F, operated at 200 kV. Soft X-ray emission spectrometer (SXES) was conducted on X-ray spectrometer SS-94000SXES mounted on JSM-7900F [52]. Electron energy loss spectrum (EELS) was recorded on a JEM ARM300F with the accelerating voltage of 200 kV.

The samples for ex-situ XRD, SXES and Raman test were treated as follows: the sample was charged/discharged at a current density of 260 mA g^{-1}. When the sample was charged/discharged to the pointed stage, the samples were removed and washed by PC to remove the electrolyte residue, and then dried in vacuum at 90 °C.

2.4. Electrochemical measurements

Electrochemical data were collected by CHI660E electrochemical workstation in a glove box filled with Ar gas at room temperature. The electrolyte was 1 M [BMIm][PF_6] ionic liquid in PC and EMC (1:1 in vol). The working windows of cyclic voltammetry (CV) and galvanostatic charge–discharge (GCD) tests of GP and GP-Li are 0–2.2 V (vs. Ag/Ag^+). Electrochemical impedance spectroscopy (EIS) measurements were carried out from 100 000 to 0.01 Hz with an alternate current amplitude of 5 mV. All electrochemical tests were performed in a three-electrode system, and non-aqueous silver ion electrode and Pt foil work as reference electrode and counter electrode, respectively.

2.5. Calculation method

Density Functional Theory (DFT) using Vienna AB-Initio simulation package (VASP) was performed for first-principle calculations. The generalized gradient approximation (GGA) with the Perdew-Burke-Ernzerhof (PBE) functional was used for depicting the electronic exchange and correlation effects. Uniform G-centered k-points meshes with a resolution of 2π*0.04 $Å^{-1}$ and Methfessel-Paxton electronic smearing were used to integrate the Brillouin zone for geometric optimization. During the whole calculation process, the cut-off energy of the simulation operation was 500 eV [38]. These settings ensure that the total energy converges to within 1 meV per atom. Structure relaxation proceeded until all forces on atoms were less than 1 meV $Å^{-1}$ and the total stress tensor was within 0.01 GPa of the target value [39]. The PF_6^- diffusion barriers in bilayer graphene were estimated by the Nudged Elastic Band (NEB) method. The intercalation energy (ΔE) of PF_6^- in bilayer graphene was estimated by the following formula:

$$\Delta E(\text{intercalation}) = E(\text{graphene} + PF_6^-) - E(\text{graphene}) - E(PF_6^-)$$

where E(graphene + PF_6^-) is the total energy of the bilayer graphene adsorbed PF_6^- ion, E(graphene) is the total energy of the bilayer graphene holding or non-holding Li and defects, and E (PF_6^-) is the total energy of the PF_6^- ion. The bilayer graphene was denoted as PF_6^--GP system, while bilayer graphene possessing a small amount of Li defect due to Li^+ pre-intercalation was denoted as PF_6^--GP-Li system.

3. Results and discussion

In order to increase the interlayer spacing of graphite for facilitating the diffusion process of anions and retain the integrity of electrode structure, a simple self-discharge treatment was used to Li^+ pre-intercalate into graphitic layers. Fig. 1(a) describes the self-discharge process and mechanism of Li^+ pre-intercalation into GP. The GP is directly in contact with the Li foil with the presence of the electrolyte. A pressure is then applied on both sides to guar-

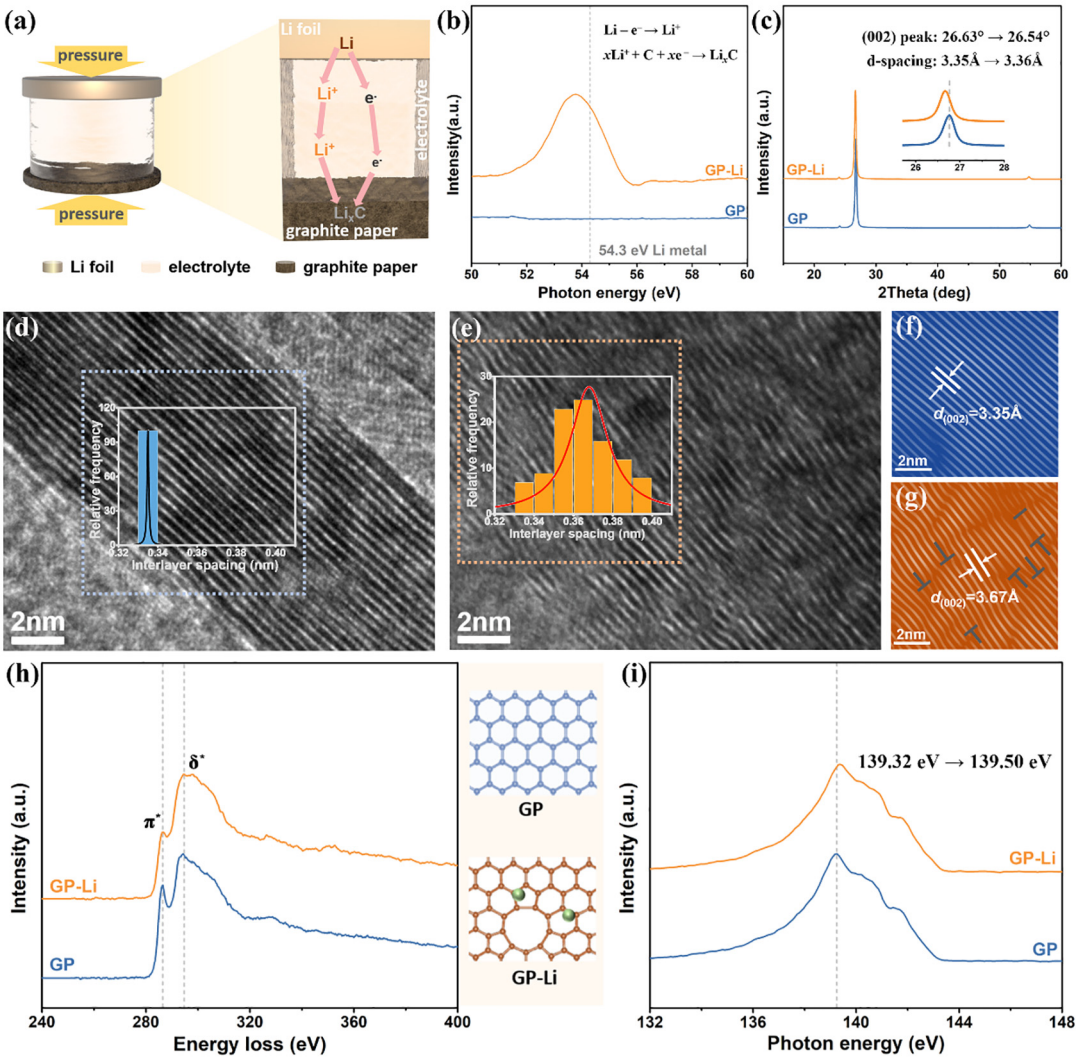

Fig. 1. Preparation strategy and physical characterizations. (a) Schematic diagram of Li^+ pre-intercalation into graphite paper. (b) Li-K_α SXES spectra comparisons of GP and Li^+ pre-intercalation graphite paper (GP-Li). (c) XRD patterns of GP and GP-Li. HRTEM image (interlayer spacing statistics diagrams) of (d) GP and (e) GP-Li. IFFT of (f) GP and (g) GP-Li . (h) K-edge core-loss EELS spectra and (i) the C-K_α SXES spectra of GP and GP-Li.

antee full contact. Due to the potential of Li metal being lower than that of GP, once the GP is contacted with Li foil, electrons spontaneously moved towards GP accompanied by Li^+ intercalation. Then the graphite paper with Li^+ pre-intercalation (GP-Li) is thereof obtained.

To investigate whether Li^+ intercalates into GP, the SXES spectra of Li element at Li-K_α spectra (50–60 eV) were conducted (Fig. 1b). The Li-K peak related to GP-Li electrode is located at ~53.75 eV, lower than that of Li metal (54.3 eV), indicating the successful intercalation of Li^+ into graphitic layers [40]. XRD measurement was carried out to investigate structural changes before and after pre-intercalation treatment (Fig. 1c). GP sample exhibits an obvious characteristic peak at 26.63°, which is corresponding to the (002) crystal plane of graphite. The (002) peak of GP-Li shifts left slightly (26.54°) after Li^+ pre-intercalation, revealing the increase of crystal plane spacing. The interlayer spacing of the graphitic layer increases from the original 3.35 Å to 3.36 Å (~0.30% expansion overall) according to the Bragg's equation ($2d\sin\theta = n\lambda$). Besides, both the FWHM (full width at half maximum) of (002) peak of the samples were unchanged before and after treatment, confirming that the pre-intercalation treatment does not change the grain size of GP. In addition, the intensity of D bond in Raman spectra (Fig. S1) increases, the I_D/I_G value arises from 0.03 (GP) to 0.12 (GP-Li), proving that the defects of graphitic structure increase and the degree of graphitization reduced after Li^+ pre-intercalation.

Electron microscopy enables characterizing the (pre-) intercalation morphological changes [53]. From SEM images, the GP (Fig. S2) presents a flake structure with alternating plane stacking, and the interspace between the smooth flakes facilitates adequate contact with electrolyte. The granular material appears on the surface of the pre-intercalated flakes (Fig. S3), which may be attributed to the local volume expansion caused by Li^+ pre-intercalation. HRTEM images display the atomic-scale features of GP and GP-Li. The interlayer spacing of two samples in the same selected area was measured (Fig. 1d and f, the sampling points are 100). The interlayer spacing distribution of the original GP is relatively concentrated, basically maintained at 0.33~0.34 nm. Whereas the interlayer spacing of GP-Li has an extended distribution at 0.33~0.40 nm, revealing that the interlayer spacing increases after the Li^+ intercalation. As can be seen from the inverse fast Fourier Transform (IFFT) in Fig. 2(f), the GP sample exhibits a

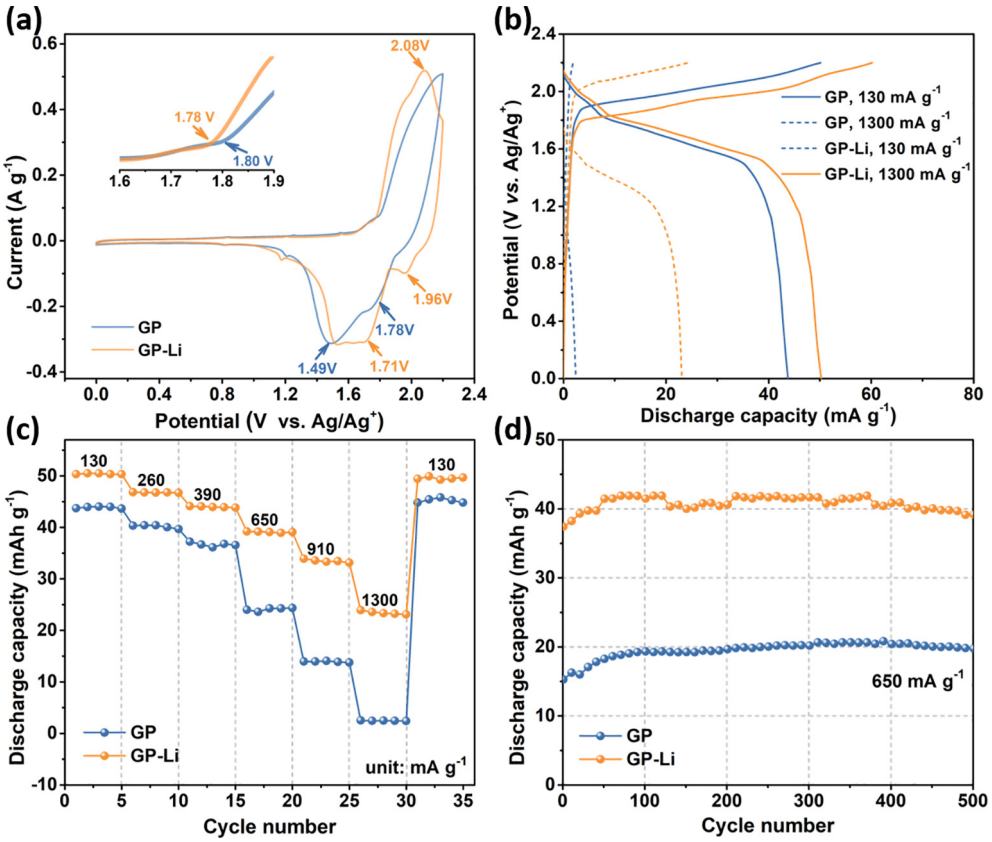

Fig. 2. Electrochemical performance comparisons between GP and GP-Li in 1 M [BMIm][PF_6] ionic liquid electrolyte. (a) CV curves at 1 mV s^{-1}. (b) GCD profiles at 130 and 1300 mA g^{-1}. (c) Rate stability at different current densities ranges from 130 to 1300 mA g^{-1} during 0–2.2 V (vs. Ag/Ag^+). (d) Long-cycling stability at 650 mA g^{-1} during 0–2.2 V (vs. Ag/Ag^+).

typical long-range ordered (002) plane arrangement with the d-spacing of 3.35 Å, which is in accord with the aforementioned XRD results. In the IFFT of GP-Li (Fig. 2g), amounts of dislocations can be observed at the (002) planes, which is consistent with an increase of disorder in Raman spectra. Besides, such arranged less ordered is accompanied by a local expansion of interlayer spacing, which may accelerate the anions diffusion between the graphitic layers. In addition, the same Li^+ pre-intercalation treatment was also performed on a HOPG. HRTEM images before and after the treatment are shown in Fig. S4. For the (002) crystal plane of HOPG, the original perfect long-range ordered structure has become less ordered; furthermore, more defects have been formed and the $d_{(002)}$-spacings increase locally. Thus, the aforementioned treatment can modify the pristinely ordered arrangement of the graphite and widen the interlayer spacings.

To explore the effect of Li^+ on the electronic structure of the graphite layer, EELS was applied (Fig. 1h). The peak at ~285 eV and a maximum with extended fine structure at ~290 eV belonged to π^* and σ^* electron transitions, respectively [41]. After Li^+ intercalation, the intensity of π^* peak decreases, suggesting that the content of sp^2 hybrid carbon decreases; the structure between graphite layers are destroyed. In addition, the fine structure in the σ^* peak of GP-Li disappears and a broad peak is generated, indicating the degradation of long-term periodicals in a graphitic base plane, correlated to the formation of non-hexagonal atomic rings [42]. The simulated diagram of the graphite base plane structure is shown in the right of Fig. 1(h). Li^+ intercalation leads to the depletion of C atoms to form void sites and carbon pentagonal rings, corresponding well to the generation of defects and the increase of interlayer spacings.

The SXES spectra of C K_α-edge were obtained to reveal whether Li^+ pre-intercalation affects the surface chemistry of GP (Fig. 1i). After the Li^+ intercalation, the C K_α-edge peak shifts towards higher energy (139.32–139.50 eV). Such change shows the average reduction state of C increase, revealing a local electron acceleration of graphite [43], which is in agreement with the behavior of Li^+ intercalation into the graphene layer. Combined with XPS spectra, the binding energy of GP-Li shifts towards the lower energy level and the sp^2 peak area decreases (Fig. S5a and Table S1), and the Li 1s signal appears (Fig. S5b), which further demonstrates that Li^+ intercalation affects the electronic structure of graphite. After cycles, Li^+ ions remain in the electrode (Fig. S6). The residual Li^+ near the surface of graphite may attract anions intercalation from the edges due to the electrostatic action [44].

To explore the influence of the GP structural change on the performance of PF_6^- storage, a series of electrochemical performance comparisons were recorded between GP and GP-Li cathodes in 1 M [BMIm][PF_6] ionic liquid electrolyte. Fig. 2(a) displays the CV curves of GP and GP-Li at a scan rate of 1 mV s^{-1}, and both the electrodes exhibit a typical CV curve of PF_6^- (de)intercalation (from) into graphitic carbon.[8] The intercalation potential of PF_6^- anions into graphene layers is ~1.80 V, and the main intercalation peak is ~2.2 V, while de-intercalation peaks appear around 1.78 and 1.49 V. After Li^+ pre-intercalation, the initial intercalation potential of PF_6^- anions into graphene layers turns to 1.78 V, 0.02 V lower than the pristine GP cathode, the decreased intercalation potential may be ascribed to the attraction of Li^+ on the surface. The main intercalation peak of GP-Li moves lefts to 2.08 V, and the de-intercalation peaks shift right to 1.96 and 1.71 V. Lower (de)intercalation peaks potential difference indicates the improved

reversibility of PF_6^- into GP-Li cathode. Besides, the area covered by the CV outline increases, confirming the enhancement of capacity, which is in agreement with the GCD curves in Fig. 2(b). The enhanced capacity can be ascribed to the improved utilization between graphene layers via the local enhancement of interlayer spacing.

To examine the anions uptake ability of GP-Li at large current, the galvanostatic discharge profiles were investigated under different current densities (Fig. 2b). The GP-Li cathode exhibits a higher discharge platform and maintains the discharge profile well at a large current. When the current density is up to 1300 mA g^{-1}, the GP-Li cathode can obtain a discharge capacity of 23 mAh g^{-1} with the typical anions de-intercalation profile, and that of GP is only 2.4 mAh g^{-1}. Table S2 and Fig. S7 display the starting voltage of discharge progress, under different current densities. The discharge voltages of GP-Li are always higher than GP, indicating that it is easier for GP-Li to release PF_6^-. Fig. 2(c) displays the rate stability at different current rates. For the GP cathode, a specific discharge capacity of 43.8 mAh g^{-1} is exhibited at 130 mA g^{-1}, and the capacity drops to 40.2, 37.1, 22.8, 13.4 and 2.4 mAh g^{-1} at 260, 390, 650, 910 and 1300 mA g^{-1}, respectively. After Li^+ pre-intercalation, GP-Li cathode displays obvious higher specific discharge capacities of 50.3, 46.7, 43.8, 39.4, 33.3 and 23.1 mAh g^{-1} at the current densities of 130, 260, 390, 650, 910 and 1300 mA g^{-1} respectively, the results show that after the pre-intercalation, the graphite interlayer utilization is improved significantly under high current density. The enhanced rate stability of GP-Li can be ascribed to the local interlayer spacing expansion and electronic structure change caused by Li^+ pre-intercalation. This superiority indicated that the pre-intercalation treatment can boost the diffusion of PF_6^- anion. In addition, the modified electrode exhibits good stability, the capacity retention rate can reach 94.6% at 650 mA g^{-1} after 500 cycles (Fig. 2d), the excellent cyclic stability can be attributed to the stably integrated structure of graphite paper. The electrochemical behavior comparisons with other anions ($TFSI^-$) intercalation into both GP and GP-Li were shown in Fig. S8. One can see that GP-Li electrode still displays lower intercalated potential and improved rate stability than GP.

To configure the influence of different structures on PF_6^- (de)intercalation process, ex-situ XRD patterns were collected. The equation of PF_6^- (de)intercalation process in graphite is expressed as follows: $xC + PF_6^- - e^- \leftrightarrow C_x(PF_6)$. When the electrode is charged, the graphite intercalation compound is generated, accompanied by an increase in interlayer spacing. When the electrode comes to discharge, the interlayer spacing returns to its original position [45,46]. The pristine GP electrode possesses a sharp (002) peak at 26.64° (Fig. 3a). When fully charged to 2.2 V, the (002) peak of GP shifts to a lower angle and splits into 25.50° and 26.37° due to the PF_6^- intercalation (Fig. S9a). When the GP electrode is discharged to 0 V, the (002) peak shifts back to 26.42°. The peak shift may be ascribed to the residue of PF_6^-. As for GP-Li electrode (Fig. 3b), at PF_6^- fully intercalation state, the typical (002) peak splits into two peaks located at 25.55° and 26.36°, respectively (Fig. S9b). In the fully charged state, the peak shift of GP-Li electrode is relatively low, due to the volume expansion accommodated by the local interlayer spacing enlargement, resulting in a lower expansion rate. When PF_6^- fully de-intercalation, the (002) peak is back to the original location, suggesting less residual of PF_6^- anions. The fewer anions residual reflects the low diffusion resistance of anions in the graphene interlayer. The Raman spectra changes of GP-Li electrode (Fig. S10) further show good structural stability. The evolution of electronic structure during the PF_6^- (de) intercalation processes can be further investigated through C-K_α SXES spectra (Fig. 3c and d). When charged to 2.2 V, the C-K_α energy shifts left; when discharged to 0 V, C-K_α energy moves back to the pristine location, the energy shift of GP and GP-Li are 0.32 and 0.48 V respectively. Such left-shift indicates the transfer of electrons from the cathode to PF_6^- during charging. The larger energy shift reveals that more PF_6^- react with cathode for energy storage, which is consistent with the enhanced capacity aforementioned.

In order to reveal the effect of Li^+ pre-intercalation on the dynamics of PF_6^- intercalating into graphene layers, the structural optimization and theoretical calculation of PF_6^- intercalation into two materials were carried out via first-principles calculations. The defect-free bilayer graphene structure of the pristine GP is shown in Fig. 3(e). A bit of defect and Li^+ residues can be observed in the GP-Li bilayer graphene model (Fig. 3f). The movement of anions through graphene layers is divided into three stages: stage Ⅰ represents PF_6^- at the open edge of graphene layers, stage Ⅱ is PF_6^- firstly intercalating into the edge of graphene layers, and stage III denotes PF_6^- inside the graphene layers. PF_6^- anions are initially induced to the outside of the graphite layer, adjacent to the opening edge. To migrate from the outside into the edge, the energy that PF_6^--GP system needs to overcome is −2.12 eV (Table S3), and for the PF_6^--GP-Li system it is −3.65 eV (noting that PF_6^- is more easily inserted into the inside GP-Li from the edge). Lower intercalation energy is probably due to the electrostatic attraction of the remaining Li^+ on the surface, suggesting that PF_6^- has lower energy to overcome when it is firstly intercalating into GP-Li, which is consistent with the aforementioned lower intercalation potential in Fig. 2(a). In addition, the diffusion barrier of anions between the graphene layers is calculated. For the PF_6^--GP system, an energy cost of 0.29 eV is needed to move from state Ⅱ to III; as to the PF_6^--GP-Li system, the energy cost is only 0.25 eV. The lower diffusion energy barrier leads to faster kinetics of PF_6^- diffusion in GP-Li graphene layers, which is possibly correlated to the local enlargement of interlayer spacing. The reduced diffusion energy barrier can explain the superior rate performance for the GP-Li in Fig. 2(c). Based on the above calculations, it appears that the enlarged interlayer spacing and the generation of defects are more favorable for PF_6^- intercalation into and diffuse between the graphene layers, which can enhance the energy storage active sites between the layers and boost the electrochemical kinetics.

Combined with theoretical calculations, electrochemical kinetic analysis was carried out to further explore the influence of Li^+ pre-intercalation on the PF_6^- storage process. A series of CV measurements for GP-Li electrode is collected at various scan rates ranging from 0.6 to 3 mV s^{-1} (Fig. 4a). With the scan rate increasing, the shape of CV curve is well preserved. The intercalation peaks shift positively and the deintercalation peaks shift negatively. These shifts are triggered by electrochemical polarization. The relationship between peak currents (i) and scan rates (v) is shown as follows [47,48]:

$$i = a v^b$$

where b is the slope of $\log(i)$ vs. $\log(v)$ fitting line, generally within the range of 0.5–1. When b approaches 0.5, the charge–discharge process is mainly controlled by ionic diffusion into the bulk, associated with the intercalation/de-intercalation process. When b is ∼1, the charge–discharge process is controlled by the diffusion on the surface, consistent with a capacitor-like behavior. The calculated b values of anions intercalation and de-intercalation into GP-Li (Fig. 4b) are 0.69 and 0.8, higher than that of GP (Fig. S11b), indicating the faster kinetics of GP-Li electrode, which may be caused by the reduction of PF_6^- diffusion barrier. When the potential is fixed (v), the current response (i) can be divided into two mechanisms: bulk diffusion controlled and surface capacitive controlled. The calculation method can be interpreted as follows [49]:

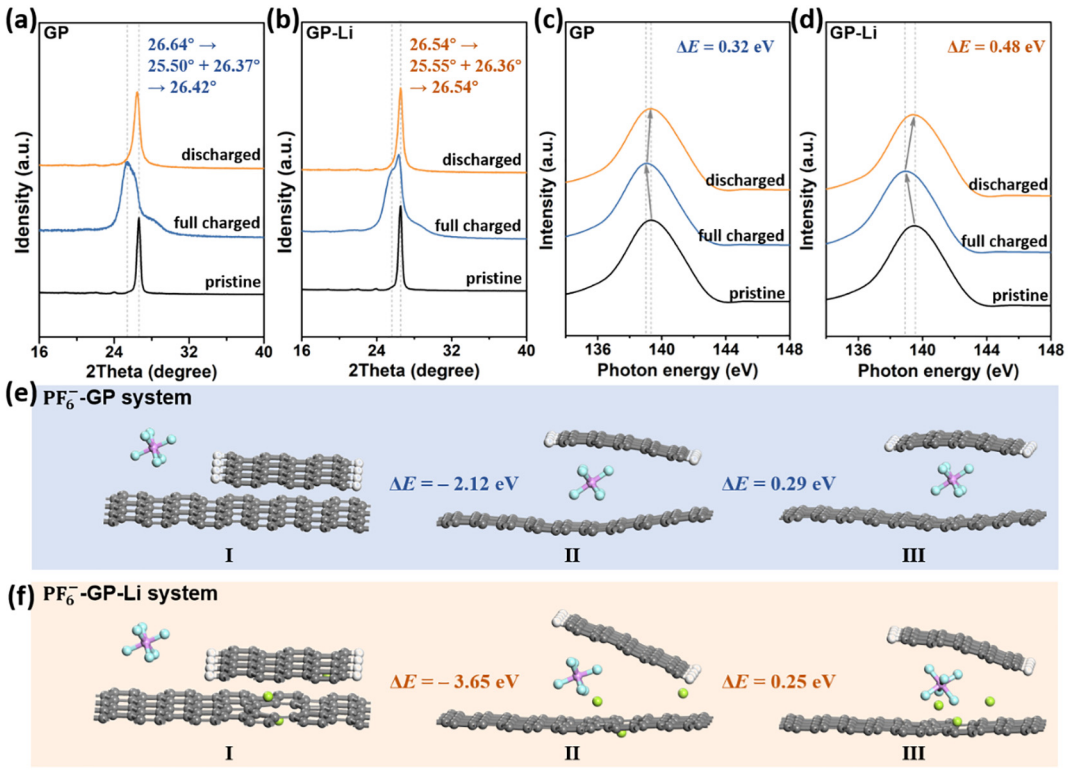

Fig. 3. Ex-situ XRD patterns and SXES spectra of different charge–discharge states. XRD patterns of (a) GP and (b) GP-Li electrode. SXES spectra of (c) GP and (d) GP-Li electrode. Theoretical calculation models of PF_6^- intercalation systems at different stages, stage Ⅰ is PF_6^- at the open edge of graphene layers, stage Ⅱ is referred to PF_6^- first intercalating into the edge of graphene layers, and stage III represents PF_6^- in graphene layers inside. (e) The PF_6^--GP and (f) PF_6^--GP-Li systems.

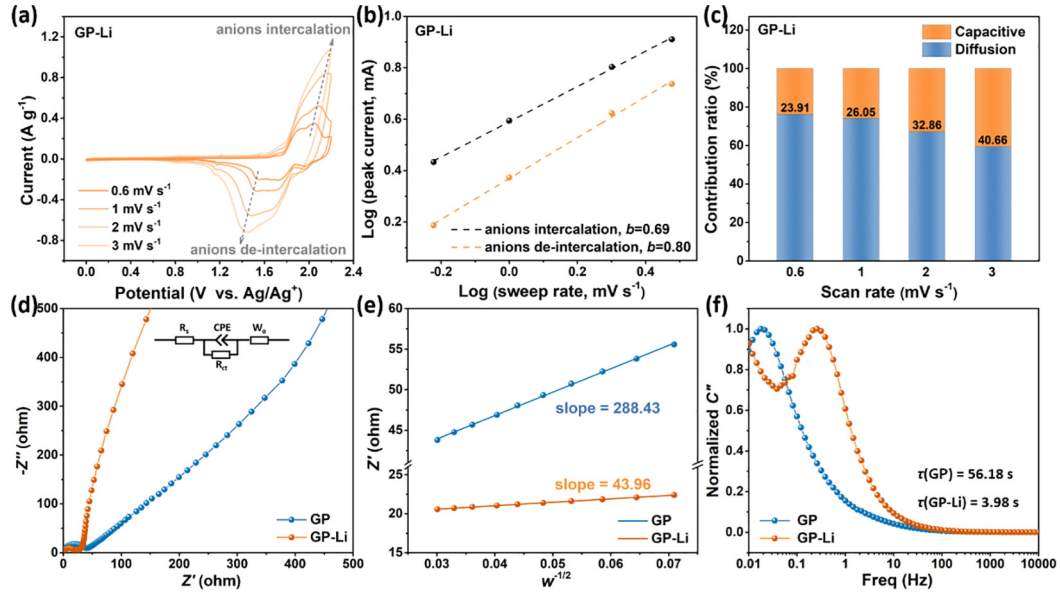

Fig. 4. Electrochemical kinetics of GP-Li cathode in 1 M [BMIm][PF_6] electrolyte. (a) The CV curves at 0.6 mV s^{-1} to 3 mV s^{-1}. (b) log *i* *vs.* log *v* plots and fitting lines at the current peak points in the anions (de)intercalation process. (c) The contribution ratio bar chart of capacitive and diffusion-controlled capacities at different scan rates. (d) Nyquist plots, (e) *Z'* as a function of $\omega^{-1/2}$ plot and (f) normalized imaginary capacitances of GP and GP-Li electrodes.

$$i(v) = k_1 v + k_2 v^{1/2}$$

where k_1 and k_2 are constants. As for GP electrode, at the scan rate of 0.6 mV s^{-1}, the capacitive contribution is 5.51%. The contribution ratio of capacitive controlled raises with the increase of the scanning rate, when the scan rate is 3 mV s^{-1}, the capacitive contribution increased to 12.88% (Fig. S11c). As for GP-Li, at 3 mV s^{-1}, a maximum capacitive-controlled ratio of 40.66% is achieved (Fig. 4c), which is higher than that of the pristine GP, revealing the faster ionic diffusion kinetics, this result is in good agreement with the DFT analysis. The capacitive-controlled ratio of the modified samples increased, confirming the enhancement of PF_6^- diffu-

sion kinetics between the graphitic layers, which is correlated to the decrease of PF_6^- diffusion barrier due to the enlargement of local interlayer spacing. Such capacitive-dominated intercalation process improves the rate stability and maintains the structural stability of the electrode material.

To further demonstrate the hypothesis that local enlargement of interlayer spacing is beneficial to easier PF_6^- intercalation and rapid diffusion, EIS tests were carried out. The impedance plots consist of a semicircle in high-frequency region and a straight line in low-frequency region. According to the fitting circuit (Fig. 4d inset), the semicircle relates to charge transfer resistance (R_{ct}), which stands for PF_6^- (de)intercalation (from) into graphitic layers. The R_{ct} of GP-Li (20.75 Ω) is lower than that of GP (42.88 Ω) (Table S4), proving that the resistance of anion intercalating into the graphitic layer is lower, which is contributed by the local interlayer spacing enlargementthat reduces the hindrance of anions diffusion. After 100 cycles, the R_{ct} of GP-Li remains lower than GP (Fig. S12). The Warburg factor (σ_w) can be obtained from the slope of the fitted line according to the following [50]

$$Z' = R_s + R_{ct} + \sigma_w \omega^{-1/2}$$

where Z' represents the real part of the complex impedance, and ω ($\omega = 2\pi f$) represents the angular frequency. The σ_w of GP-Li cathode is 43.96, much lower than that of GP-Li (Fig. 4e), indicating that the graphitic layers of GP-Li hold faster PF_6^- diffusion. Minimum relaxation time constant τ (the minimum time required to release all energy with efficiency > 50%, $\tau = 1/f$) can be further used to verify the ion diffusion rate (Fig. 4f). The smaller τ of GP-Li (3.98 s) further reveals the improved anion diffusion kinetics [51]. All the above kinetic analysis is in good agreement with the aforementioned theoretical calculation and experimental data.

Due to the low diffusion kinetics of large-size anions between the graphitic layers, the layered structure of graphite cannot be fully utilized, further hindering the development of DIBs. In this case, the direct contact method of Li^+ pre-intercalation is proposed to improve the overall performance of GP in DIBs. The residual Li^+ ions between the graphite layers may induce PF_6^- to intercalate into the graphitic layers, leading to the reduction of the intercalation energy barrier. It is probably the reason for the decrease of the intercalation potential. The local interlayer spacing enlargement and generation of defects provide a faster PF_6^- diffusion and reduce the anion accumulation, leading to lower PF_6^- diffusion barrier, thus enhancing the rate stability. The simple self-discharge method improves the slow diffusion kinetics of PF_6^- in stacked graphite, and combines with high stability, high flexibility and integrative graphite paper electrode. Such merits are of great significance for manufacturing flexible DIB energy storage with fast charge–discharge and high stability performance.

4. Conclusions

In summary, the utilization rate of GP cathode in DIBs is improved by Li^+ pre-intercalation via self-discharge mechanism. After Li^+ pre-intercalation, the interlayer spacing enlarges locally, which promotes the diffusion kinetics of PF_6^- anion. Besides, the residual Li^+ in the electrode materials may induce the intercalation of PF_6^-. The corresponding theoretical simulation proves that Li^+ pre-intercalation reduces the intercalation energy and diffusion barrier of anions. As a result, the obtained GP-Li electrode exhibits a discharge capacity of 23.1 mAh g^{-1} at a high current of 1300 mA g^{-1}, and the capacity retention rate reaches 94.8% at a current of 650 mA g^{-1} after 500 cycles. Our pre-treatment method provides a novel insight for enhancing the diffusion kinetics of anions in carbon-based DIB cathode. Nowadays, the study of the graphitic cathode is still in its infancy. In the future, the energy storage mechanism of the graphitic cathode can be investigated with more advanced characterization methods, so as to accurately design the high resistance and superior stability cathode. Towards the practical application of DIBs, there is space for matching between the cathode–anode voltage and capacity.

Declaration of competing interest

The authors declare that they have no known competing financial interests or personal relationships that could have appeared to influence the work reported in this paper.

Acknowledgments

This work is financially supported by the National Natural Science Foundation of China (51932003, 51872115), the 2020 International Cooperation Project of the Department of Science and Technology of Jilin Province (20200801001GH) and the Project supported by State Key Laboratory of Luminescence and Applications (KLA-2020-05).

Appendix A. Supplementary data

Supplementary data to this article can be found online at https://doi.org/10.1016/j.jechem.2022.04.009.

References

[1] H. Yang, T. Qin, T. Deng, W. Zhang, W. Zheng, Energy Fuels 34 (2020) 15701–15713.
[2] X. Zhou, Q. Liu, C. Jiang, B. Ji, X. Ji, Y. Tang, H.M. Cheng, Angew. Chem. Int. Ed. 59 (2020) 3802–3832.
[3] W. Li, X. Wu, Electrochem. Sci. Adv. 2 (2021) 2100127.
[4] Y. Wang, N. An, L. Wen, L. Wang, X. Jiang, F. Hou, Y. Yin, J. Liang, J. Energy Chem. 55 (2021) 391–419.
[5] W. Zhang, D. Wang, W. Zheng, J. Energy Chem. 41 (2020) 100–106.
[6] T. Kim, W. Song, D.Y. Son, L.K. Ono, Y. Qi, J. Mater. Chem. A 7 (2019) 2942–2964.
[7] X. Shi, S. Yu, T. Deng, W. Zhang, W. Zheng, J. Energy Chem. 44 (2020) 13–18.
[8] S. Rothermel, P. Meister, G. Schmuelling, O. Fromm, H.W. Meyer, S. Nowak, M. Winter, T. Placke, Energy Environ. Sci. 7 (2014) 3412–3423.
[9] X. Tong, X. Ou, N. Wu, H. Wang, J. Li, Y. Tang, Adv. Energy Mater. 11 (2021) 2100151.
[10] W. Han, M. Lu, J. Chen, H. Li, H. Li, B. Zhang, W. Zhang, W. Zheng, J. Mater. Chem. A 8 (2020) 16265–16270.
[11] X. Shi, W. Zhang, J. Wang, W. Zheng, K. Huang, H. Zhang, S. Feng, H. Chen, Adv. Energy Mater. 6 (2016) 1601378.
[12] X. Zhang, Y. Tang, F. Zhang, C.S. Lee, Adv. Energy Mater. 6 (2016) 1502588.
[13] L. Sui, X. Shi, T. Deng, H. Yang, H. Liu, H. Chen, W. Zhang, W. Zheng, J. Energy Chem. 37 (2019) 7–12.
[14] S. Wang, J. Tu, J. Xiao, J. Zhu, S. Jiao, J. Energy Chem. 28 (2019) 144–150.
[15] L. Fan, Q. Liu, S. Chen, Z. Xu, B. Lu, Adv. Energy Mater. 7 (2017) 1602778.
[16] M. Sheng, F. Zhang, B. Ji, X. Tong, Y. Tang, Adv. Energy Mater. 7 (2017) 1601963.
[17] H. Wang, H. Wang, Y. Li, Y. Wang, Z. Si, J. Energy Chem. 58 (2021) 9–16.
[18] N. Li, Y. Xin, H. Chen, S. Jiao, H. Jiang, W. Song, D. Fang, J. Energy Chem. 29 (2019) 122–128.
[19] T. Placke, A. Heckmann, R. Schmuch, P. Meister, K. Beltrop, M. Winter, Joule 2 (2018) 2528–2550.
[20] G. Wang, M. Yu, J. Wang, D. Li, D. Tan, M. Loffler, X. Zhuang, K. Mullen, X. Feng, Adv Mater. 30 (2018) 1800533.
[21] W. Li, Y. Li, X. Liu, Z. Gu, H. Liang, X. Zhao, J. Guo, X. Wu, Adv. Funct. Mater. 2 (2022) 2201038.
[22] W. Li, H. Liang, X. Hou, Z. Gu, X. Zhao, J. Guo, X. Yang, X. Wu, J. Energy Chem. 50 (2020) 416–423.
[23] J. Ge, L. Fan, A.M. Rao, J. Zhou, B. Lu, Nat. Sustain. 5 (2022) 225–234.
[24] Z. Liu, Y. Yang, S. Liang, B. Lu, J. Zhou, Small Struct. 2 (2021) 2100119.
[25] L. Fan, Y. Hu, A.M. Rao, J. Zhou, Z. Hou, C. Wang, B. Lu, Small Methods 5 (2021) 2101131.
[26] Y. Wang, Y. Zhang, S. Dong, W. Zhou, P. Lee, Z. Peng, C. Dang, P.H.L. Sit, J. Guo, D. Y.W. Yu, Adv. Energy Mater. (2022) 2103360.
[27] A. Kotronia, H.D. Asfaw, C. Tai, M. Hahlin, D. Brandell, K. Edström, ACS Appl. Mater. Interfaces 13 (2021) 3867–3880.
[28] A. Ejigu, L.W. Le Fevre, K. Fujisawa, M. Terrones, A.J. Forsyth, R.A.W. Dryfe, ACS Appl. Mater. Interfaces 11 (2019) 23261–23270.
[29] L. Zhang, L. Chen, H. Luo, X. Zhou, Z. Liu, Adv. Energy Mater. 7 (2017) 1700034.

[30] H. Chen, F. Guo, Y. Liu, T. Huang, B. Zheng, N. Ananth, Z. Xu, W. Gao, C. Gao, Adv. Mater. 29 (2017) 1605958.
[31] H. Yang, X. Shi, T. Deng, T. Qin, L. Sui, M. Feng, H. Chen, W. Zhang, W. Zheng, ChemElectroChem 5 (2018) 3612–3618.
[32] E. Zhang, W. Cao, B. Wang, X. Yu, L. Wang, Z. Xu, B. Lu, Energy Storage Mater. 11 (2018) 91–99.
[33] C. Zhan, X. Zeng, X. Ren, Y. Shen, R. Lv, F. Kang, Z. Huang, J. Energy Chem. 42 (2020) 180–184.
[34] F. Wang, J. Yi, Y. Wang, C. Wang, J. Wang, Y. Xia, Adv. Energy Mater. 4 (2014) 1300600.
[35] X. Shi, Y. Yang, G. Zhu, Ceram. Int. 46 (2020) 13835–13840.
[36] Z. Li, B. Niu, Y. Liu, J. Li, F. Kang, Electrochim. Acta 263 (2018) 68–75.
[37] J.V. Rani, V. Kanakaiah, T. Dadmal, M.S. Rao, S. Bhavanarushi, J. Electrochem. Soc. 160 (2013) A1781–A1784.
[38] Z. Zhao, W. Zhang, M. Liu, D. Wang, X. Wang, L. Zheng, X. Zou, Z. Wang, D. Li, K. Huang, W. Zheng, Energy Environ. Mater. 5 (2022), https://doi.org/10.1002/eem1002.12342.
[39] T. Dong, W. Yi, T. Deng, T. Qin, X. Chu, H. Yang, L. Zheng, S.J. Yoo, J.G. Kim, Z. Wang, Y. Wang, W. Zhang, W. Zheng, Energy Environ. Mater. 5 (2022), https://doi.org/10.1002/eem2.12262.
[40] Y. Domi, H. Usui, A. Ando, K. Nishikawa, H. Sakaguchi, ACS Appl. Energy Mater. 3 (2020) 8619–8626.
[41] K.H. Kouhei, N. Kushita, Ultramicroscopy 35 (1991) 289–293.
[42] K. Niwase, Mater. Sci. Eng. A 400–401 (2005) 101–104.
[43] I. Mihara, Z.L. An, A. Kinoshita, M. Hirai, M. Kusaka, M. Iwami, Appl. Surf. Sci. 159–160 (2000) 197–200.
[44] H. Michael, F. Iacoviello, T.M.M. Heenan, A. Llewellyn, J.S. Weaving, R. Jervis, D. J.L. Brett, P.R. Shearing, J. Electrochem. Soc. 168 (2021) 010507.
[45] J.A. Seela, J.R. Dahn, J. Electrochem. Soc. 147 (2000) 892–898.
[46] T.E. Sutto, T.T. Duncan, T.C. Wong, Electrochim. Acta 54 (2009) 5648–5655.
[47] Z. Pan, T. Qin, W. Zhang, X. Chu, T. Dong, N. Yue, Z. Wang, W. Zheng, J. Energy Chem. 68 (2022) 42–48.
[48] T. Qin, X. Chu, T. Deng, B. Wang, X. Zhang, T. Dong, Z. Li, X. Fan, X. Ge, Z. Wang, P. Wang, W. Zhang, W. Zheng, J. Energy Chem. 48 (2020) 21–28.
[49] V. Augustyn, J. Come, M.A. Lowe, J.W. Kim, P.L. Taberna, S.H. Tolbert, H.D. Abruña, P. Simon, B. Dunn, Nat. Mater. 12 (2013) 518–522.
[50] M. Fan, Y. Chen, Y. Xie, T. Yang, X. Shen, N. Xu, H. Yu, C. Yan, Adv. Funct. Mater. 26 (2016) 5019–5027.
[51] X. Yang, C. Cheng, Y. Wang, L. Qiu, D. Li, Science 341 (2013) 534–537.
[52] T. Qin, W. Zhang, Y. Ma, W. Zhang, T. Dong, X. Chu, T. Li, Z. Wang, N. Yue, H. Liu, L. Zheng, X. Fan, X. Lang, Q. Jiang, W. Zheng, Energy Stor. Mater. 45 (2022) 33–39.
[53] T. Qin, D. Wang, X. Zhang, Y. Wang, N.E. Drewett, W. Zhang, T. Dong, T. Li, Z. Wang, T. Deng, Z. Pan, N. Yue, R. Yang, K. Huang, S. Feng, R. Huang, W. Zheng, Energy Stor. Mater. 36 (2021) 376–386.